Lateral migration and equilibrium shape and position of a single red blood cell in bounded Poiseuille flows

Lingling Shi, Tsorng-Whay Pan, and Roland Glowinski

Phys. Rev. E **86**, 056308 — Published 13 November 2012

DOI: 10.1103/PhysRevE.86.056308

Lateral migration and Equilibrium Shape and Position of a Single Red Blood Cell in Bounded Poiseuille Flows

Lingling Shi, Tsorng-Whay Pan*, and Roland Glowinski
Department of Mathematics, University of Houston, Houston, Texas 77204, USA

October 25, 2012

Abstract

Lateral migration and equilibrium shape and position of a single red blood cell (RBC) in bounded two-dimensional Poiseuille flows are investigated by using an immersed boundary method (IBM). An elastic spring model is applied to simulate the skeleton structure of RBC membrane. We focus on studying the properties of lateral migration of a single RBC in Poiseuille flows by varying the initial position, the initial angle, the swelling ratio (s^*), the membrane bending stiffness of RBC (k_b), the maximum velocity of fluid flow ($u_{\max}$), and the degree of confinement. The combined effect of the deformability, the degree of confinement and the shear gradient of the Poiseuille flow make the RBC migrate toward a certain cross-sectional equilibrium position, which lies either on the centerline of the channel or off centerline. For $s^* > 0.8$, the speed of the migration at the beginning decreases as increasing the swelling ratio s^*. But for $s^* < 0.8$, the speed of the migration at the beginning is an increasing function of the swelling ratio s^*. Two motions of oscillation and vacillating-breathing (swing) of RBC are observed. The distance Y_d between the cell mass center of the equilibrium position and the centerline of the channel increases as increasing the Reynolds number Re and reaches a peak, then decreases as increasing Re. The peak of the Reynolds number is a decreasing function of the swelling ratio ($s^* < 1.0$). The cell membrane energy of the equilibrium position is an increasing function as the Reynolds number Re increases. The slipper shape cell is more stable than the parachute shape one in the sense that the energy stored in the former is lower than that in the latter. For a given Re, the bigger the swelling ratio ($s^* < 1.0$), the lower the cell membrane energy.

Keywords lateral migration, equilibrium shape, equilibrium position, red blood cell, elastic spring model, immersed boundary method, Poiseuille flow.

1 Introduction

The rheological property of the red blood cells (RBCs) is a key factor of the blood flow characteristics in microvessels due to their large volume fraction (40%−45%), so called hematocrit (Hct), in the whole blood. The normal RBC has a biconcave disk with a major diameter about 8 μm, and its membrane composing of a lipid bilayer underlined by a spectrin network of cytoskeletal proteins is highly deformable so that RBC can change its shape when an external force is acting on it and return to the biconcave resting shape after the removal of the force [1]. Studying the dynamical behaviors (such as deformability and the motion) of the RBCs suspending in fluid flow becomes an essential problem in biomedical and biochemical industries and these studies may serve as a useful and practical method in designing the cells separating microfluid devices based on their mechanical properties such as size, deformability and etc [2]. Many researchers in mathematics, physics and mechanics, biology, and medicine have studied this problem by using various entities, such as particles, drops, capsules, vesicles and RBCs theoretically [3, 4], experimentally [5, 6, 7, 8, 9, 10, 11], and numerically [7, 12, 13, 14, 15, 16, 17, 18, 20, 21, 22, 23]. But most studies have been limited to the Stokes flow or the cells are restricted to the sphere or ellipse. Here we examine the deformable cell behavior in the flow with inertial effect, and the biconcave cell is also included.

*Corresponding author. E-mail address: pan@math.uh.edu

Several numerical methods have been developed to study the cross-stream migration of these entities in Poiseuille flows. S. Mortazavi *et al.* studied that the cross-stream migration of a deformable drop in a Poiseuille flow at finite Reynolds numbers by using the finite difference/front tracking method and reported that the motion of the drop strongly depends on the viscosity ratio of its inside and outside, for ratio 1.0 it moves away from the the center until halted by the wall repulsion [13]. Pozrikidis studied the motion of spherical, oblate ellipsoidal and biconcave capsules in tube flow by using boundary element method and observed that spherical capsules slowly migrate to the tube centerline, and oblate and biconcave capsules develop parachute and slipper shapes, respectively [15]. B. Kaoui *et al.* studied the cross-streamline noninertial migration of a suspended vesicle in an unbounded (bounded by Coupier *et al.* [7]) Poiseuille flow at low Reynolds numbers by using the boundary integral method and found that the vesicle deforms and migrates toward the center of the flow [16]. M. Yoshino and T. Murayama applied the lattice Boltzmann method (LBM) to study the motion of a viscoelastic body in a Poiseuille flow and observed that the equilibrium position is very close to the centerline for a low elasticity and it is at a certain position between the centerline and the wall for a larger elasticity [14]. Danker *et al.* investigated the effect of viscosity ratio on migration of vesicles in a Poiseuille flow by theoretical analysis and predicted coexistence of two types of shapes: bulletlike shape and parachutelike shape [22]. In most of the above studies, the deformability of these entities was included, but no inertial effect on the cross-stream migration was considered.

The effect of the inertia on the lateral motion of particles in a Poiseuille flow was first documented experimentally by Segré and Silberberg [8, 9]. They observed that rigid neutrally buoyant particles migrate away from both the wall and the centerline, forming a concentrated layer at about half the distance between the wall and the centerline. By using spherical particles and drops, Karnis *et al.* further studied this effect and found that the deformable drops migrate to the centerline if their viscosity is low [10, 11]. T. Ko *et al.* investigated the migration and multiple equilibrium positions of a single particle in Poiseuille flows and observed that the equilibrium height of a neutrally buoyant particle between the wall and the channel centerline depends on the Reynolds number [12]. Some theoretical studies of the effect of the inertia have been limited to spherical particles [4]. Recently, the inertial migration of an elastic capsule in a bounded Poiseuille flow at a finite Reynolds number was investigated by Shin [18]. But the initial shape of the capsule is limited to either a circle or an ellipse. Doddi *et al* studied the lateral migration of a three-dimensional deformable capsule in a Poiseuille flow based on a mixed finite-difference/Fourier transform method for the flow solver and a front-capsule method for the deformable interface and reported that the capsules without bending migrate toward the centerline [21].

In this paper, inertial migration and equilibrium position and shape of a cell with different initial shape (convex and biconcave) in bounded two-dimensional Poiseuille flows have been studied by numerical simulation. We have used an immersed boundary method combined with the elastic spring model [24] in which the fluid motion is computed by using an operator splitting technique and finite element method [25, 26] with a fixed regular triangular mesh so that a faster solver can be used to solve the fluid flow [27, 28, 29, 30]. In Ref. [20], the validation of the methodology was presented on the RBC deformation in linear shear flow by comparing with the simulation results obtained by the lattice-Boltzmann method in Ref. [31]. Here several important factors have been examined for the inertial migration of a single RBC in Poiseuille flows: the swelling ratio (s^*), the membrane bending stiffness of RBC (k_b), the maximum velocity of fluid flow ($u_{\max}$), and the degree of confinement (the ratio of the cell's effective radius R_0 to the channel half height w). The combined effect of the deformability, the degree of confinement and the shear gradient of the Poiseuille flow make the RBC migrate toward a certain cross-sectional equilibrium position, which lies either on the centerline of the channel or off centerline. For $s^* > 0.8$, the speed of the migration at the beginning decreases as increasing the swelling ratio s^*. But for $s^* < 0.8$, the speed of the migration at the beginning is an increasing function of the increasing the swelling ratio s^*. Two motions of oscillation and vacillating-breathing (swing) of RBC are observed. The distance Y_d between

the cell mass center of the equilibrium position and the centerline of the channel is monotonic decreasing as s^* increases in a narrower channel. For the elliptic shape cell and the almost circle cell with larger values of k_b , the distance Y_d increases with increasing Re, reaches a peak at about $Re = 40$ and decreases as Re increases.

The scheme of this paper is as follows: We discuss the elastic spring model and numerical methods in Section 2. In Section 3, we study the lateral migration properties of a single RBC in Poiseuille flows, the effect of the membrane bending stiffness of RBC (k_b), the maximum velocity of fluid flow ($u_{\max}$), and the degree of confinement, and the diagram of equilibrium shapes, positions and the associated energy versus Re. The conclusions are summarized in Section 4.

2 Model and method

A RBC with the viscosity of the cytoplasm the same as that of the blood plasma is suspended in a fluid domain Ω filled with blood plasma which is incompressible, and Newtonian. For some $T > 0$, the governing equations for the fluid-cell system are the Navier-Stokes equations

$$\rho\left(\frac{\partial \mathbf{u}}{\partial t} + \mathbf{u}\cdot\nabla\mathbf{u}\right) = -\nabla p + \mu\triangle\mathbf{u} + f \text{ in } \Omega\times(0,T), \tag{1}$$

$$\nabla\cdot\mathbf{u} = 0 \text{ in } \Omega\times(0,T). \tag{2}$$

Equations (1) and (2) are completed by the following boundary and initial conditions:

$$\mathbf{u} = 0 \text{ on the top and bottom of } \Omega \text{ and } \mathbf{u} \text{ is periodic in the } x_1 \text{ direction}, \tag{3}$$

$$\mathbf{u}(x,0) = \mathbf{u}_0(x) \text{ in } \Omega \tag{4}$$

where $\mathbf{u}$ and p are the fluid velocity and pressure, respectively, ρ is the fluid density, and μ is the fluid viscosity, which is assumed to be constant for the entire fluid. In Eq. (1), f is a body force which is the sum of f_p and f_B, where f_p is the pressure gradient pointing in the x_1 direction and f_B accounts for the force acting on the fluid-cell interface. In Eq. (4), $\mathbf{u}_0(x)$ is the initial fluid velocity.

In this paper, the Navier-Stokes equations for fluid flow have been solved by using an operator splitting technique and finite element method [25, 26] with a regular triangular mesh so that the faster solver from FISHPAK by Adams *et al.* [32] can be used to solve the fluid flow. The motion of the RBCs in the fluid flow is simulated by combining the immersed boundary method [33, 34, 35] and the elastic spring model for the RBC membrane [24] (also see [27, 29, 30]).

2.1 Elastic spring model for the RBC membrane

The deformability and the elasticity of the RBC are due to the skeleton architecture of the membrane. A two-dimensional elastic spring model in Ref. [24] is considered in this paper to describe the deformable behavior of the RBCs. Based on this model, the RBC membrane can be viewed as membrane particles connecting with the neighboring membrane particles by springs, as shown in Figure 1. Energy stores in the spring due to the change of the length l of the spring with respect to its reference length l_0 and the change in angle θ between two neighboring springs. The total energy of the RBC membrane, $E = E_l + E_b$, is the sum of the total energy for stretch and compression and the total energy for the bending which, in particular, are

$$E_l = \frac{k_l}{2}\sum_{i=1}^{N}(\frac{l_i - l_0}{l_0})^2 \tag{5}$$

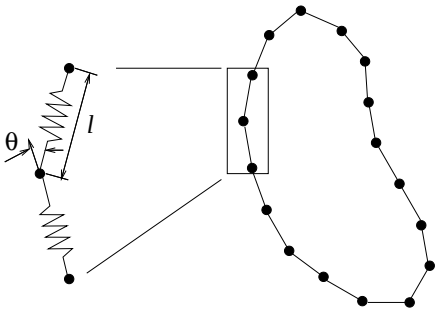

Figure 1: The elastic spring model of the RBC membrane.

and

$$E_b = \frac{k_b}{2}\sum_{i=1}^{N} tan^2(\theta_i/2). \tag{6}$$

In equations (5) and (6), N is the total number of the spring elements, and k_l and k_b are spring constants for changes in length and bending angle, respectively.

In the process of creating the initial shape of RBCs described in Ref. [24], the RBC is assumed to be a circle of radius $R_0 = 2.8$ μm initially. The circle is discretized into $N = 76$ membrane particles so that 76 springs are formed by connecting the neighboring particles. The shape change is stimulated by reducing the total area of the circle through a penalty function

$$\Gamma_s = \frac{k_s}{2}(\frac{s - s_e}{s_e})^2, \tag{7}$$

where s and s_e are the time dependent area of the RBC and the equilibrium area of the RBC, respectively, and the total energy is modified as $E + \Gamma_s$. Based on the principle of virtual work the force acting on the ith membrane particle now is

$$\mathbf{F}_i = -\frac{\partial(E + \Gamma_s)}{\partial \mathbf{r}_i}, \tag{8}$$

where $\mathbf{r}_i$ is the position of the ith membrane particle. When the area is reduced, each RBC membrane particle moves on the basis of the following equation of motion:

$$m\ddot{\mathbf{r}}_i + \gamma\dot{\mathbf{r}}_i = \mathbf{F}_i. \tag{9}$$

Here, $\dot{()}$ denotes the time derivative, and m and γ represent the membrane particle mass and the membrane viscosity of the RBC. The position $\mathbf{r}_i$ of the ith membrane particle is solved by discretizing Eq. (9) via a second order finite difference method. The total energy stored in the membrane decreases as the time elapses. The final shape of the RBC is obtained as the total energy is minimized [27]. The area of the final shape has less than 0.001% difference from the given equilibrium area s_e and the length of the perimeter of the final shape has less than 0.005% difference from the circumference of the initial circle. The value of the swelling ratio of a RBC in this paper is defined by $s^* = s_e/(\pi R_0^2)$.

2.2 Immersed boundary method

The immersed boundary method developed by Peskin, e.g., [33, 34, 35], is employed in this study because of its distinguishing features in dealing with the problem of fluid flow interacting with a flexible fluid-structure interface. Based on the method, the boundary of the deformable structure is discretized spatially into a set of boundary nodes. The force located at the immersed boundary node $\mathbf{X} = (X_1, X_2)$ affects the nearby fluid mesh nodes $\mathbf{x} = (x_1, x_2)$ through a two-dimensional discrete δ function $D_h(\mathbf{X}-\mathbf{x})$:

$$\mathbf{f}_B(\mathbf{x}) = \sum \mathbf{F}_i D_h(\mathbf{X}_i - \mathbf{x}) \quad \text{for } |\mathbf{X}_i - \mathbf{x}| \le 2h, \tag{10}$$

where h is the uniform finite element mesh size and

$$D_h(\mathbf{X}-\mathbf{x}) = \delta_h(X_1 - x_1)\delta_h(X_2 - x_2) \tag{11}$$

with the one-dimensional discrete δ functions being

$$\delta_h(z) = \begin{cases} \frac{1}{8h}\left[3 - 2|z|/h + \sqrt{1 + 4|z|/h - 4(|z|/h)^2}\right], & |z| \le h, \\ \frac{1}{8h}\left[5 - 2|z|/h - \sqrt{-7 + 12|z|/h - 4(|z|/h)^2}\right], & h \le |z| \le 2h, \\ 0, & \text{otherwise.} \end{cases} \tag{12}$$

The movement of the immersed boundary node $\mathbf{X}$ is also affected by the surrounding fluid and therefore is enforced by summing the velocities at the nearby fluid mesh nodes $\mathbf{x}$ weighted by the same discrete δ function:

$$\mathbf{U}(\mathbf{X}) = \sum h^2 \mathbf{u}(\mathbf{x_j}) D_h(\mathbf{X} - \mathbf{x_j}) \quad \text{for } |\mathbf{X} - \mathbf{x_j}| \le 2h. \tag{13}$$

After each time step, the position of the immersed boundary node is updated by

$$\mathbf{X}_{t+\Delta t} = \mathbf{X}_t + \Delta t \mathbf{U}(\mathbf{X}_t). \tag{14}$$

Remark. At each time step, via operator splitting, we solve a sequence of subproblems, namely a degenerated quasi-Stokes problem, the membrane motion, the advection problem, and the diffusion problem as in Ref. [30]. We keep the conservation of area given in Eq. (7) when computing membrane force in Eq. (8) since the divergence free condition is enforced in a weak sense through the finite element method used in the computations.

3 Simulation results and discussions

In Ref. [20], as a benchmarking test, the steady inclination angles of the tank treading of two different degrees of confinement for five values s^* in shear flow are shown and compared with the simulation results in Ref. [31]. In this paper, the lateral migration properties of a single RBC in Poiseuille flows have been investigated by varying the swelling ratio (s^*), the membrane bending constant of RBC (k_b), the maximum velocity of fluid flow ($u_{\max}$), and the degree of confinement. Two motions of oscillation and vacillating-breathing (swing) of the RBC are observed in both narrow (100×10 μm^2) and wide (100×20 μm^2) channels considered here.

The values of parameters for modeling cells are same with [29, 30] as follows: The bending constant is $k_b = 5 \times 10^{-10}$ Nm, the spring constant is $k_l = 5 \times 10^{-8}$ Nm, and the penalty coefficient is $k_s = 10^{-5}$ Nm. The cells are suspended in blood plasma which has a density $\rho = 1.00$ g/cm^3 and a dynamical viscosity $\mu = 0.012$ g/(cms). The viscosity ratio which describes the viscosity contrast of the inner and outer fluid of the RBC membrane is fixed at 1.0. The computational domain is a two dimensional horizontal channel. To obtain a Poiseuille flow, a constant pressure gradient is prescribed as a body force. In addition, periodic conditions are imposed at the left and right boundary of the domain. The Reynolds number is defined by $Re = \rho UH/\mu$ where U is the average velocity in the channel, and H is the height of the channel.

3.1 Initial position and angle tests

First we consider the effect of the initial position and the angle φ of the long axis of the cell with respect to the centerline on the lateral migration.

Given the same initial angle φ, the effect of different initial positions has been investigated in a Poiseuille flow with the fluid domain 100×20 μm^2. The pressure gradient is set to as a constant so that the Reynolds number of the Poiseuille flow without cell is about 0.8333. The initial velocity is zero

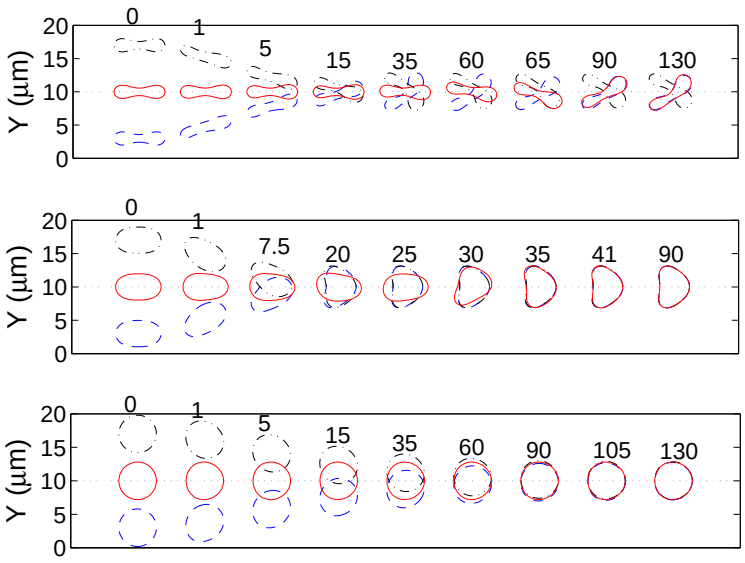

Figure 2: (Color online). The snapshots of the cell migration with three different initial positions of s^* = 0.481 (top), 0.9 (middle), and 1.0 (bottom) at different time (ms).

everywhere. The grid resolution for the computational domain is 64 grid points per 10 μm. Migrations of the RBC with s^* = 0.481, 0.9, and 1.0 for three different initial positions (5,3), (5,10), and (5,17) are shown in Figure 2. The cells with the initial positions (5,3) and (5,17) deform and migrate to the centerline of the microchannel where steady states are reached. The cell reaches the slipper shape for s^* = 0.481, the parachute shape for s^* = 0.9 and the slightly bullet-like shape as its equilibrium shape for the circular case of s^* = 1.0, respectively. The deformation of the cell with the initial positions (5,3) and (5,17) is greater than that with the initial position (5, 10) after the cells are placed in the fluid flow. The three cells with different initial positions migrate to the same equilibrium position and attain the same shape. The cell initial position does lead to different initial behavior, but the final position and shape are not related with the initial positions of the RBC.

The effect of the angle is also studied for the biconcave shape cell with s^* = 0.481 and the elliptic shape cell with s^* = 0.9, respectively. Figure 3 presents the snapshots of the cell migration with the angles $\varphi = 0^o$, 45^o and 90^o. By the combination effect of the wall and the deformability, the cell with the initial angle $\varphi = 0^o$ deforms and rotates counterclockwise with an angle about 45^o, the cell with $\varphi = 90^o$ deforms and rotates clockwise with an angle about 45^o, and the cell with the initial angle $\varphi = 45^o$ deforms and almost keeps the same angle. The deformation of the cells with the initial angles $\varphi = 0^o$ and 90^o is greater than that with the initial angle 45^o after the cells are released in the fluid flow. As shown in Figure 3, it takes almost the same time (5 ms) for these three cells with different initial angles to reach about the same shape and height in the flow. Then they keep migrating in the flow with no significant different in shape and height. The initial angle has influence on the cell initial behavior, but has no significant effect on its motion after its release into the fluid flow for a while.

3.2 Lateral migration of a single RBC in a Poiseuille flow

3.2.1 Effect of the swelling ratio

Here we present the simulation results of a single RBC in a Poiseuille flow with the fluid domain 100 $\times$ 20 μm^2. The pressure gradient is set to as a constant so that the Reynolds number of the Poiseuille flow without cell is about 0.8333. The initial velocity is zero everywhere. The grid resolution for the

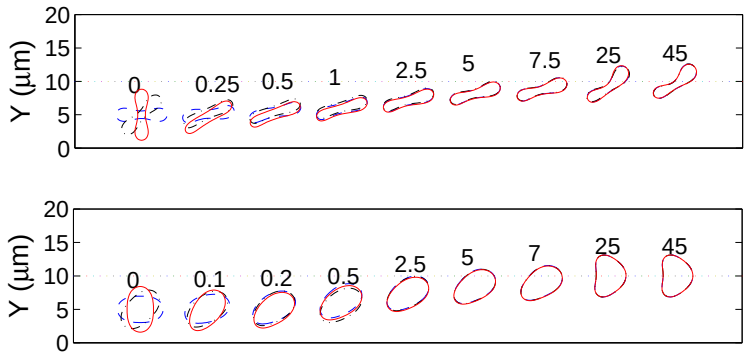

Figure 3: (Color online). The snapshots of the cell migration with three different initial angles $\varphi = 0^o$, 45^o, and 90^o of $s^* = 0.481$ (top) and 0.9 (bottom) at different time (ms).

computational domain is 64 grid points per 10 μm. Seven different shapes of the cells ($s^* = 0.481$, 0.6, 0.7, 0.8, 0.9, 0.95 and 1.0) have been studied and the simulation results are shown in Figure 4. The initial position of the mass center of the single cell is located at (5,3) as in Figure 3. The initial angle is $\varphi = 0$. The cells deform after they are released close to the bottom wall and migrate toward higher fluid velocity field, i.e. toward the centerline of the channel and reach their equilibrium shapes and positions, respectively. The average velocities of the fluid flow with the cells are 4.9562, 4.9546, 4.9528, 4.9504, 4.9501, 4.9515, and 4.953 cm/s for $s^* = 0.481$, 0.6, 0.7, 0.8, 0.9, 0.95, and 1.0, respectively. The associated Reynolds numbers are 0.826, 0.8258, 0.8255, 0.8251, 0.825, 0.8253, and 0.8255. Whiling migration, the biconcave shape cell with $s^* = 0.481$, 0.6, 0.7, and 0.8 moves to lateral location characterized by lower shear rates accompanied with damped vacillating-breathing (swing) motion. The damped speed is an inverse proportion function with the swelling ratio s^*. The equilibrium shapes for various swelling ratio are shown in Figure 4. The equilibrium positions are at or near the centerline and the distance Y_d is monotonic decreasing to zero as increasing the swelling ratio from 0.481 to 1.0 since the shape is changing from the asymmetric slipper shape to the symmetric shape. The energy stored in the cell membrane of the equilibrium cell is also monotonic decreasing as increasing the swelling ratio from 0.481 to 1.0. The extra energy due to the cell deformation shown in Figure 4 also indicates that the shape of $s^* = 0.8$ has been changed the most. As shown in Figure 4, for $s^* > 0.8$, the speed of the migration at the beginning decreases as increasing the swelling ratio s^*. This result agrees very well qualitatively with the experimental results reported in Ref. [7]. But for $s^* \leq 0.8$, which has not been studied in Ref. [7], the speed of the migration at the beginning is an increasing function of the swelling ratio s^*. The critical swelling ratio $s^* = 0.8$ for having biconcave shape also plays a role here concerning the migration velocity at the beginning. For $s^* > 0.8$, the deformability is weaker for higher value of s^* due to the lack of the excess circumference. But for $s^* \leq 0.8$, the excess circumference is more than enough for the cell to deform and the cell of larger s^* can interact more with the faster flow region due to the larger cell area and then migrates faster.

3.2.2 Effect of the membrane bending stiffness of RBC

To study the effect of the bending constant, we have kept the same values of k_l and k_s and considered three different values of the bending constants, which are $0.1k_b$, $1k_b$, and $10k_b$, and other parameters are same as in Section 3.2.1. The capillary numbers C_a are 135.337, 13.533, and 1.353 corresponding to the bending constants 0.1kb, 1kb, and 10kb, respectively. Here $C_a = \mu \mathrm{G_r R_0}^3/\mathrm{B}$, where μ, $\mathrm{G_r}$, $\mathrm{R_0}$ and B represent the plasma viscosity, the shear rate of fluid flow based on the gradient of the velocity

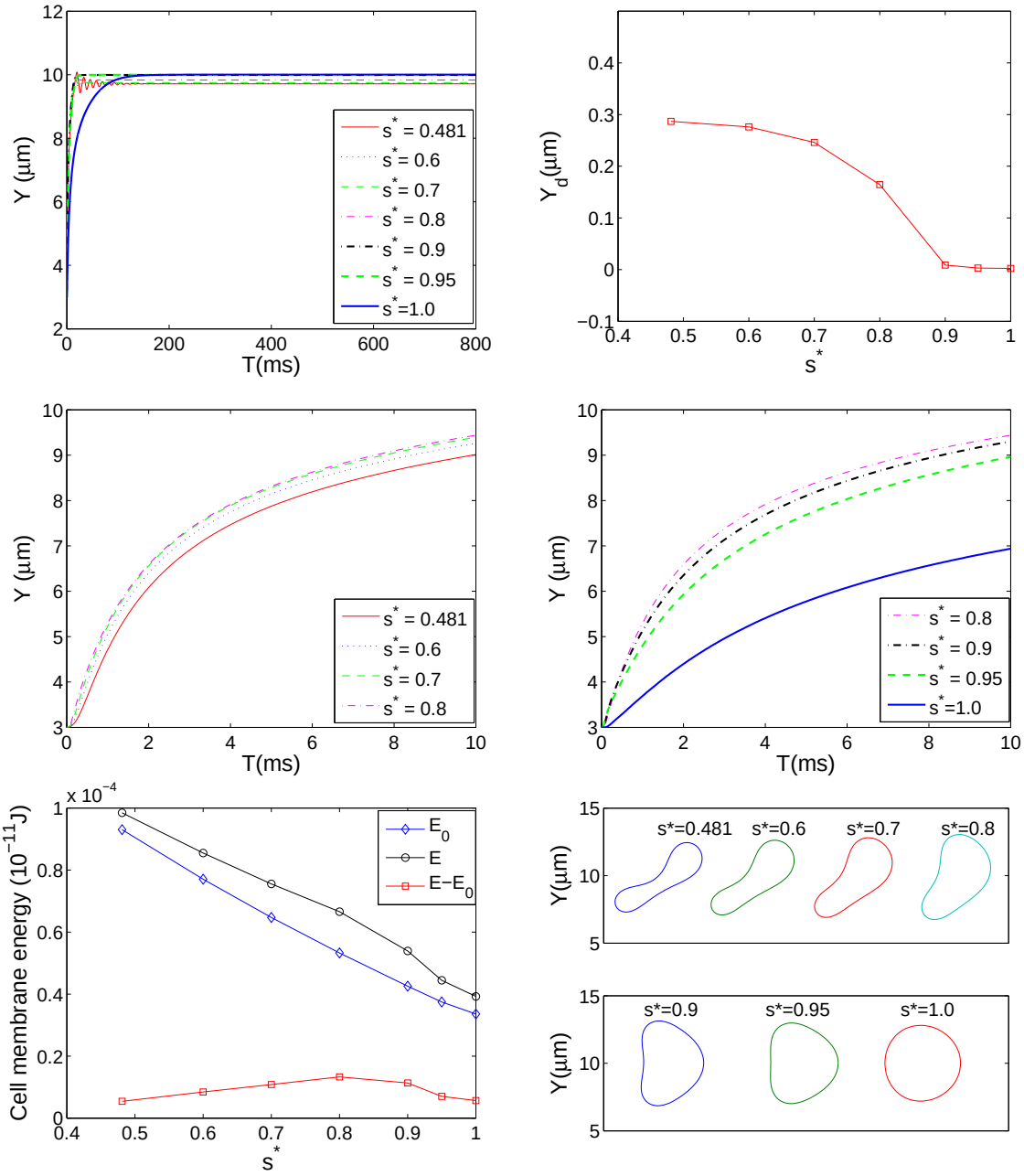

Figure 4: (Color online). The history of the position of the cell mass center (top left) and the distance Y_d as a function of the swelling ratio s^* for the degree of confinement $R_0/w = 0.28$ (top right). The history of the position of the cell mass center at the beginning 10 ms of $s^* = 0.481$, 0.6, 0.7, and 0.8 (middle left) and $s^* = 0.8$, 0.9, 0.95, and 1.0 (middle right). The initial cell membrane energy E_0, the cell membrane energy of the equilibrium state E, and the energy difference $E - E_0$ (bottom left) and the equilibrium shapes for various swelling ratios $s^* = 0.481$, 0.6, 0.7, 0.8, 0.9, 0.95, and 1.0 (bottom right).

at the wall, the effective radius of the cell, and the bending coefficient, respectively. The snapshots of the cell migration in Poiseuille flows for $s^* = 0.481$, 0.9, and 1.0 with these bending constants are shown in Figure 5. The red asterisk denotes the same point on the cell membrane during the entire simulation. The histories of the position of the cell mass centers are displayed in Figure 6. For the above three bending constants, the cells migrate toward the equilibrium height close to the centerline of the channel. Different deformability led by the different bending constants presents different dynamical properties during the cell migration. For the lower bending constant $0.1k_b$, the cell with $s^* = 0.9$ migrates to the equilibrium height faster than the other two as shown in Figure 6. The parachute shape is obtained for both the biconcave shape cell and the elliptic shape cell, and a slightly bulletlike shape is observed for the circular shape cell. For the bending constant $1k_b$, the cell with $s^* = 0.9$ also migrates faster to the equilibrium height. But both the biconcave shape cell and the elliptic shape cell exhibit damped vacillating-breathing after they are released in the fluid flow as indicated in Figure 6. The equilibrium location of the biconcave shape cell is 0.2863 μm away from the centerline due to its asymmetric equilibrium shape (slipper shape). For the higher bending constant $10k_b$, both the biconcave shape cell and the elliptic shape cell exhibit damped oscillation until they attain the equilibrium states aligning themselves at an angle with the direction of the flow as shown in Figure 5 (g) and (h). The damping rate of the elliptical shape cell is again bigger than that of the biconcave shape cell as shown by the history of the angle θ in Figure 6. Concerning the vacillating-breathing behavior in a Poiseuille flow, it was first observed without considering the lateral migration in the study [20]. To obtain this kind of behavior, the bending constant needs to be large enough with respect to the velocity $u_{\max}$ so that the cell can not be deformed into either a symmetric parachute or a bullet-like shape at the centerline. In another word, the cell shape has to be a long body shape in the central region of the channel as shown in Figure 5 $(d), (g)$ and (h) so that when the mass center of the cell moves up and down, its inclination angle oscillates since the portion of the membrane closer to the wall moves slower than that in the central region does. When the mass center finally settles to a steady height, the oscillation disappears.

3.2.3 Effect of the maximum velocity

The effect of $u_{\max}$ on the lateral migration of a single cell in Poiseuille flows has been investigated. In the simulations, we have kept other parameters same as in Section 3.2.1. We observed that $u_{\max}$ plays a critical role on the migration, the deformation, the equilibrium position and shape of the cell. The higher $u_{\max}$, the faster the cell deforms. So when the velocity of the cell migration is higher, it reaches the equilibrium shape more quickly. During the migration, both the biconcave shape cell and the elliptic shape cell exhibit a damped vacillating-breathing motion after the cell reached the centerline of the channel for lower $u_{\max}$ and the vacillating-breathing motion damps out quickly for the elliptic shape cell. When the equilibrium shape is symmetric with respect to the centerline of the channel such as ellipse, parachute shape and bullet shape, the mass center lies in the centerline of the channel, otherwise, when the equilibrium shape is asymmetric such as slipper shape, the mass center settles between the centerline and the wall. The histories of the cell mass centers are shown in Figure 7. The distance Y_d as a function of the Reynolds number Re and the corresponding equilibrium shapes for three different swelling ratio $s^* = 0.481$, 0.9, and 1.0 are displayed in Figures 8 and 9, respectively.

For the biconcave shape cell with $s^* = 0.481$, a slipper shape as its equilibrium shape is obtained for various $u_{\max}$. For the elliptic shape cell with $s^* = 0.9$, a slipper shape as its equilibrium shape is observed for $u_{\max} < 7.5$ cm/s ($Re < 0.83$), a parachute shape as its equilibrium shape is observed for 7.5 cm/s $\leq u_{\max} \leq 230$ cm/s ($0.83 \leq Re \leq 25.56$) and $u_{\max} \geq 410$ cm/s ($Re \geq 45.56$), and an asymmetric shape as its equilibrium shape is observed for 230 cm/s $< u_{\max} < 410$ cm/s ($25.56 < Re < 45.56$). For the circular shape cell with $s^* = 1.0$, a (slightly) bulletlike shape as its equilibrium shape is obtained for $u_{\max} < 60$ cm/s ($Re < 6.67$) and $u_{\max} \geq 900$ cm/s ($Re \geq 100$), and an asymmetric shape as its

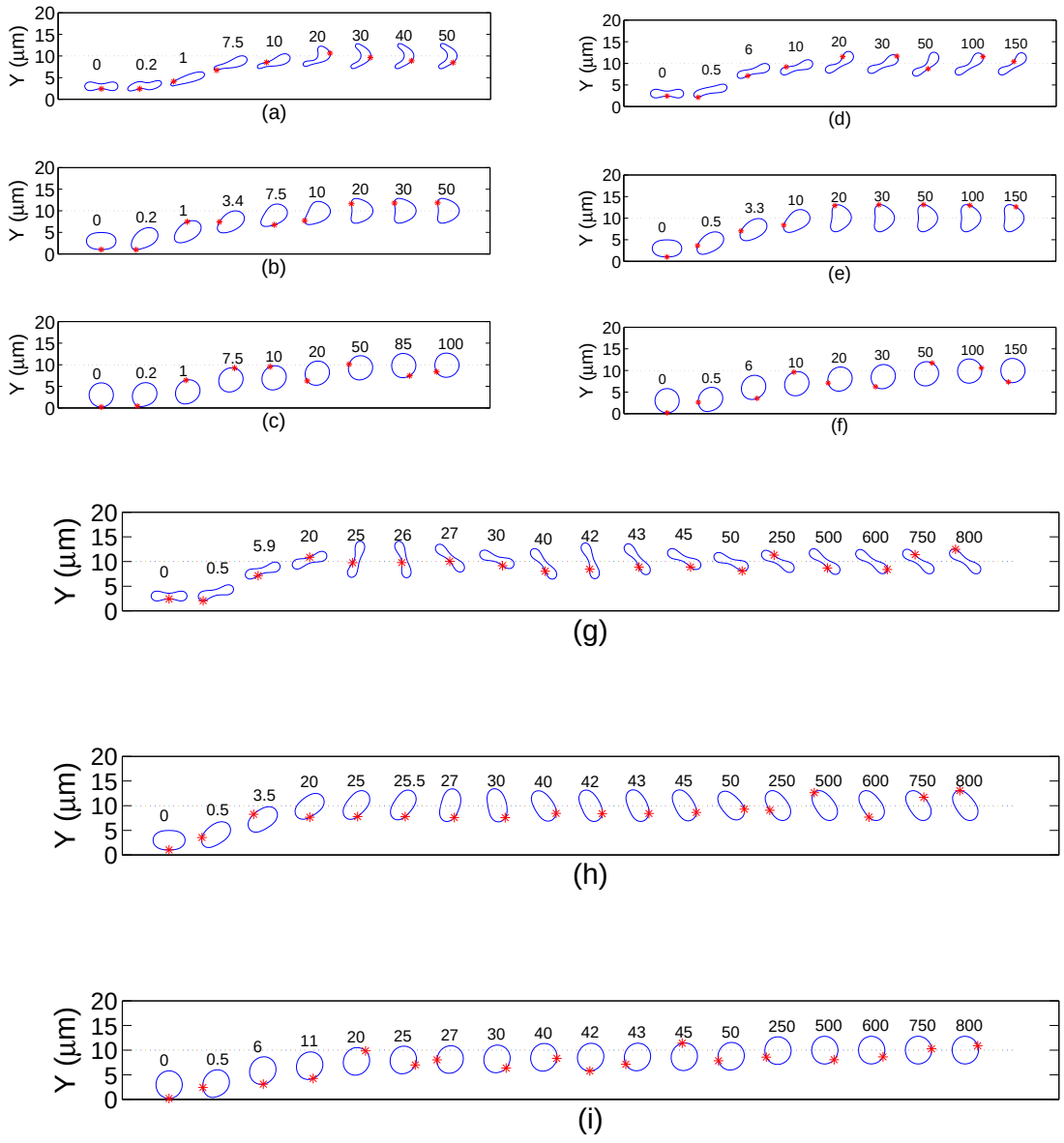

Figure 5: (Color online) The snapshots of the cell migration in Poiseuille flows for s^*=0.481, 0.9, and 1.0 with different bending constants at different time (ms): (a) $s^* = 0.481$ and $0.1k_b$, (b) $s^* = 0.9$ and $0.1k_b$, (c) $s^* = 1.0$ and $0.1k_b$, (d) $s^* = 0.481$ and $1k_b$, (e) $s^* = 0.9$ and $1k_b$, (f) $s^* = 1.0$ and $1k_b$, (g) $s^* = 0.481$ and $10k_b$, (h) $s^* = 0.9$ and $10k_b$, (i) $s^* = 1.0$ and $10k_b$. The red asterisk denotes the same node point on the cell membrane.

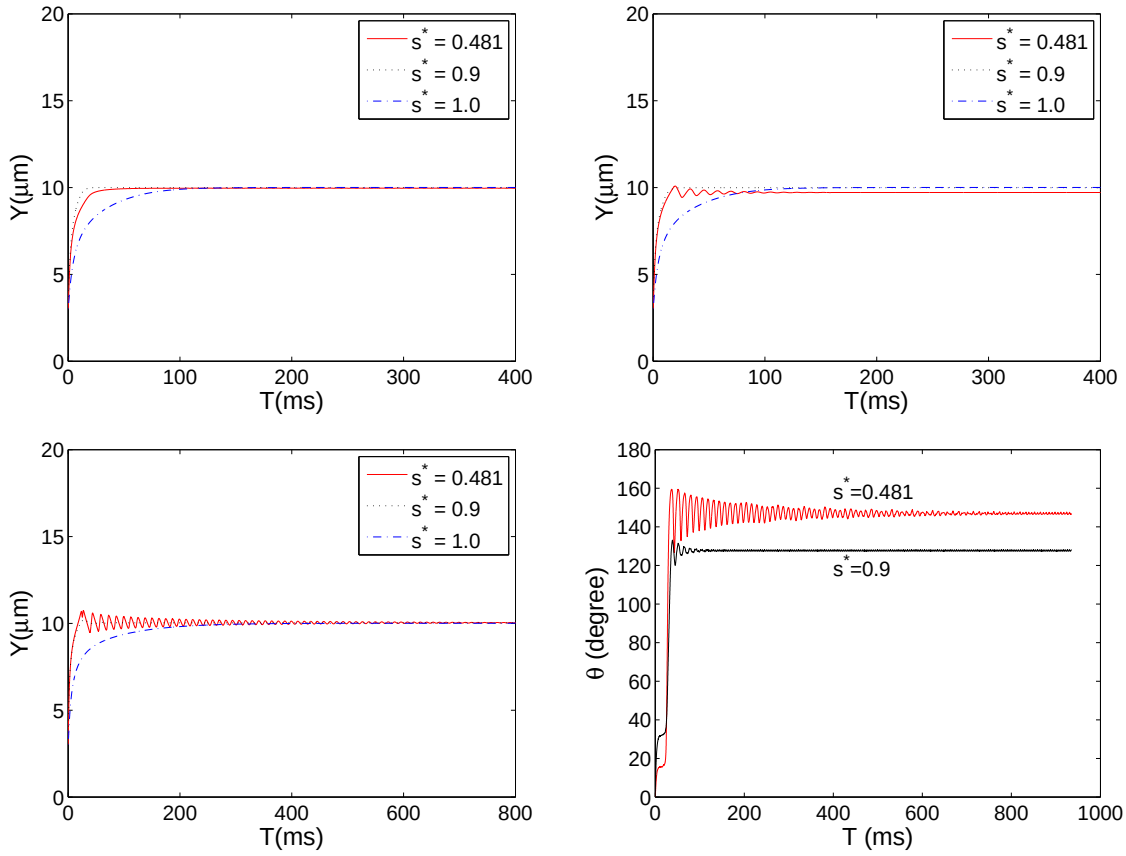

Figure 6: (Color online). The history of the position of the cell mass center for various bending constants $0.1k_b$ (top left), $1k_b$ (top right), and $10k_b$ (bottom left). The history of the angle between the long axis of cell and the horizontal line for the bending constant $10k_b$ (bottom right).

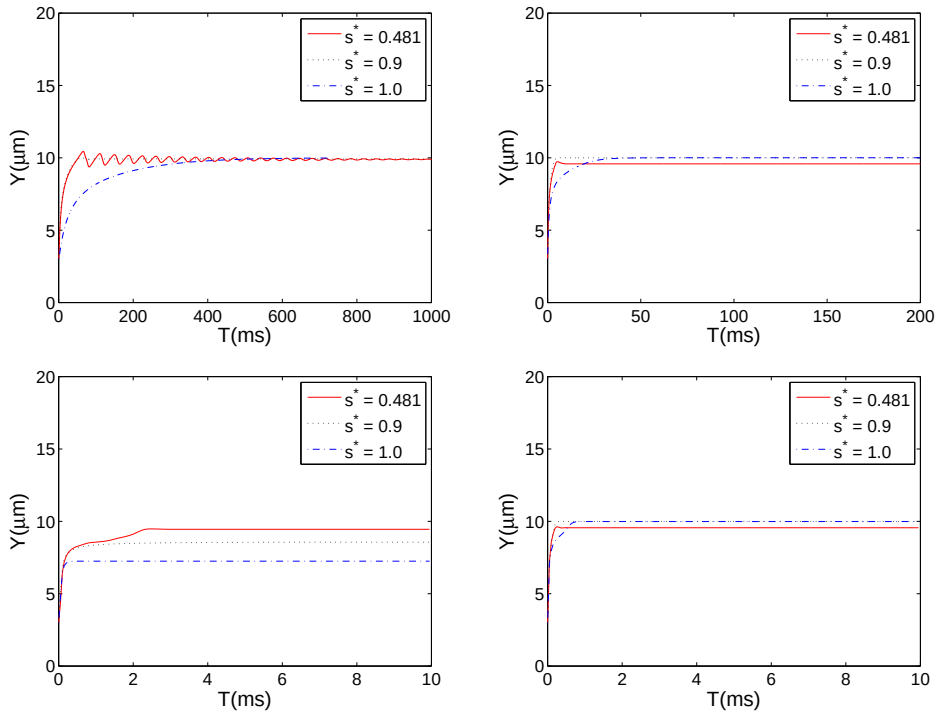

Figure 7: (Color online). The history of the position of the cell mass center for various $u_{\max}$=2.5 (top left), 30 (top right), 240 (bottom left), and 900 cm/s (bottom right). The associated Reynolds numbers Re are 0.278, 3.33, 26.67, and 100.

equilibrium shape is observed for 60 cm/s $\leq u_{\max} <$ 900 cm/s ($6.67 \leq Re < 100$).

The asymmetric shape (slipperlike shape) of vesicle in an unbounded Poiseuille flow at zero Reynolds number has been studied by Kaoui *et al.* [3], and the similar results of vesicle also mentioned in [36, 37, 38]. But the difference is that our simulation results show the cell of $s^* = 0.9$ and 1.0 can stay away from the centerline with an asymmetric equilibrium shape as increasing value of $u_{\max}$ and then shift back to the centerline with a symmetric parachute and bulletlike shape with enough higher $u_{\max}$ as shown in Figures 7 and 9. The above migration of the cell of $s^* = 0.9$ and 1.0 depends mainly on two lift forces in the narrow channel considered here: one is a positive force toward the channel center generated by the inertial effect of the wall, and the other is a negative force toward the wall generated by the shear gradient of the Poiseuille flow. The cell migrates toward the channel center when $u_{\max}$ is very slow since, besides the cell deformability, the effect of the wall is stronger than that of the shear gradient of the flow then the positive lift force from the wall is larger than the negative lift force when the cell is closer to the wall. As $u_{\max}$ is larger, the effect of wall becomes weaker comparing the effect of velocity profile of the fluid flow, the composite force becomes negative, and then the equilibrium position shifts away from the centerline. When $u_{\max}$ increases further, the curvature of velocity profile of the fluid flow becomes very small, the negative lift force generated by the shear gradient of the Poiseuille flow decreases. So the cell migrates to the centerline of the channel for much higher $u_{\max}$ in a narrower channel considered here. The similar tendency for the capsule was reported in Ref. [18]. For a neutrally buoyant particle of an elliptic shape moving in a bounded Poiseuille flow, the mass center also moves to the centerline of the higher enough $u_{\max}$ in [19] under the same reason.

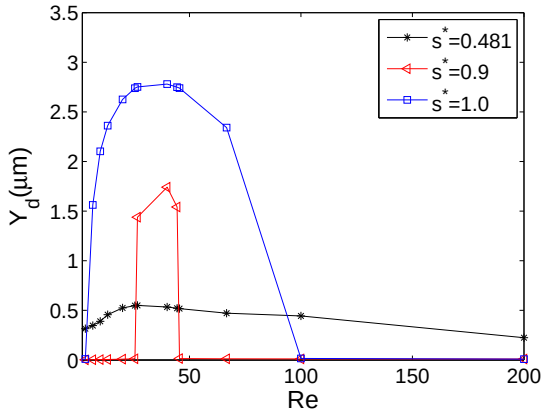

Figure 8: (Color online). The distance Y_d between the cell mass center of the equilibrium position and the centerline of the channel as a function of the Reynolds number Re.

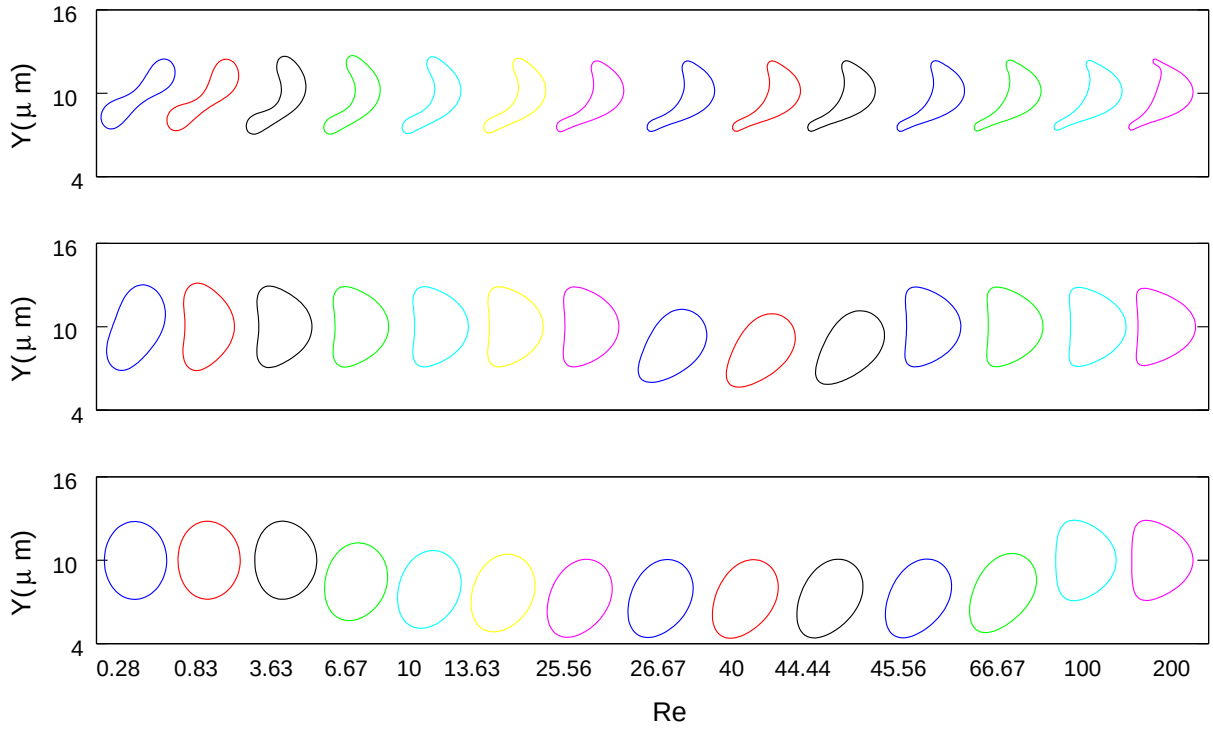

Figure 9: (Color online). The equilibrium position and shape of $s^* = 0.481$, 0.9, and 1.0 (from top to bottom) with the $u_{\max} = 2.5$, 7.5, 30, 60, 90, 120, 230, 240, 360, 400, 410, 600, 900 and 1800 cm/s (from left to right) and the associated Reynolds numbers Re are 0.28, 0.83, 3.33, 6.67, 10, 13.33, 20, 26.67, 40, 44.44, 45.56, 66.67, 100, and 200.

3.2.4 The effect of the degree of confinement

Finally, we compare the equilibrium position and shape of the RBC in Poiseuille flows by varying the degree of confinement. In this section, we consider two different degrees of confinement $R_0/w = 0.56$ (100×10 μm^2) and 0.28 (100×20 μm^2) and six swelling ratios $s^* = 0.481$, 0.6, 0.7 , 0.8, 0.9, and 1.0. Simulation results are reported in Figures 10 and 11 for these two degrees of confinement, respectively. In Figure 10, the Reynolds number Re is between 0 and 0.5 for the degree of confinement $R_0/w = 0.56$. The distance Y_d increases as increasing the Reynolds number Re and reaches a peak, then decreases as increasing Re for $s^* = 0.481$, 0.6, 0.7, and 0.8. The peak of the Reynolds number (0.1389, 0.1111, 0.0833, and 0.0694) is a decreasing function of the swelling ratio s^* (0.481, 0.6, 0.7, and 0.8). After the distance Y_d reaches its peak, the cell equilibrium position shifts back to the centerline of the channel and the equilibrium shape becomes parachute shape for $s^* \leq 0.9$ and bulletlike shape for $s^* = 1.0$. The diagram of the equilibrium shape in Figure 10 is similar to the simulation results in Ref. [3]. In Figure 11, the Reynolds number Re is between 0 and 5 for a less degree of confinement $R_0/w = 0.28$. The distance Y_d increases as increasing the Reynolds number Re and reaches a peak, then decreases as increasing Re for $s^* = 0.481$, 0.6, 0.7 , and 0.8. The peak of the Reynolds number (2.222, 1.333, 0.833, 0.667, and 0.444) is a decreasing function of the swelling ratio s^* (0.481, 0.6, 0.7, 0.8, and 0.9). The distance Y_d is almost zero for the swelling ratio $s^* = 1.0$ due to its symmetric shape. For the wider channel, it needs higher $u_{\max}$ to obtain a symmetric shape for the cell of smaller values of the swelling ratio s^*, especially for the one of $s^* = 0.481$. It indicates that the degree of confinement is also important for obtaining the parachute shape in a bounded Poiseuille flow. In general, for the bigger degree of confinement, the distance Y_d is highly related to the equilibrium shape: Y_d is zero for the symmetric equilibrium shape such as parachute shape and bulletlike shape, but Y_d is nonzero for the asymmetric equilibrium shape such as slipper shape.

Given a swelling ratio s^*, the cell membrane energy of the equilibrium position is an increasing function as the Reynolds number Re increases. The slipper shape cell is more stable than the parachute shape one in the sense that the energy stored in the former is lower than that in the latter. This is another way to explain why the slipper shape is a favorable shape in a Poiseuille flow besides the one based on reducing the lag by assuming a slipper shape discussed in Ref. [3]. For a given Re, the bigger the swelling ratio ($s^* < 1.0$), the lower the cell membrane energy. The membrane energy of the cell of $s^* = 1.0$ behaves differently from the others for the both degrees of confinement considered here. The corresponding equilibrium shapes of the various swelling ratios $s^* = 0.481$, 0.6, 0.7 ,0.8, 0.9, and 1.0 are shown in Figure 10 (bottom).

4 Conclusions

Lateral migration and equilibrium shape and position of a single red blood cell (RBC) in bounded two-dimensional Poiseuille flows are investigated by using an immersed boundary method (IBM). An elastic spring model is applied to simulate the skeleton structure of RBC membrane. We focus on studying the properties of inertial migration of a single RBC in Poiseuille flows by varying the initial position, the initial angle, the swelling ratio (s^*), the membrane bending stiffness of RBC (k_b), the maximum velocity of fluid flow ($u_{\max}$), and the degree of confinement. The combined effect of the deformability, the degree of confinement and the shear gradient of the Poiseuille flow make the RBC migrate toward a certain cross-sectional equilibrium position, which lies either on the centerline of the channel or off centerline. For $s^* > 0.8$, the speed of the migration at the beginning decreases as increasing the swelling ratio s^*. But for $s^* < 0.8$, the speed of the migration at the beginning is a increasing function of the swelling ratio s^*. Two motions of oscillation and vacillating-breathing (swing) of RBC are observed. The distance Y_d between the cell mass center of the equilibrium position and the centerline of the channel increases as

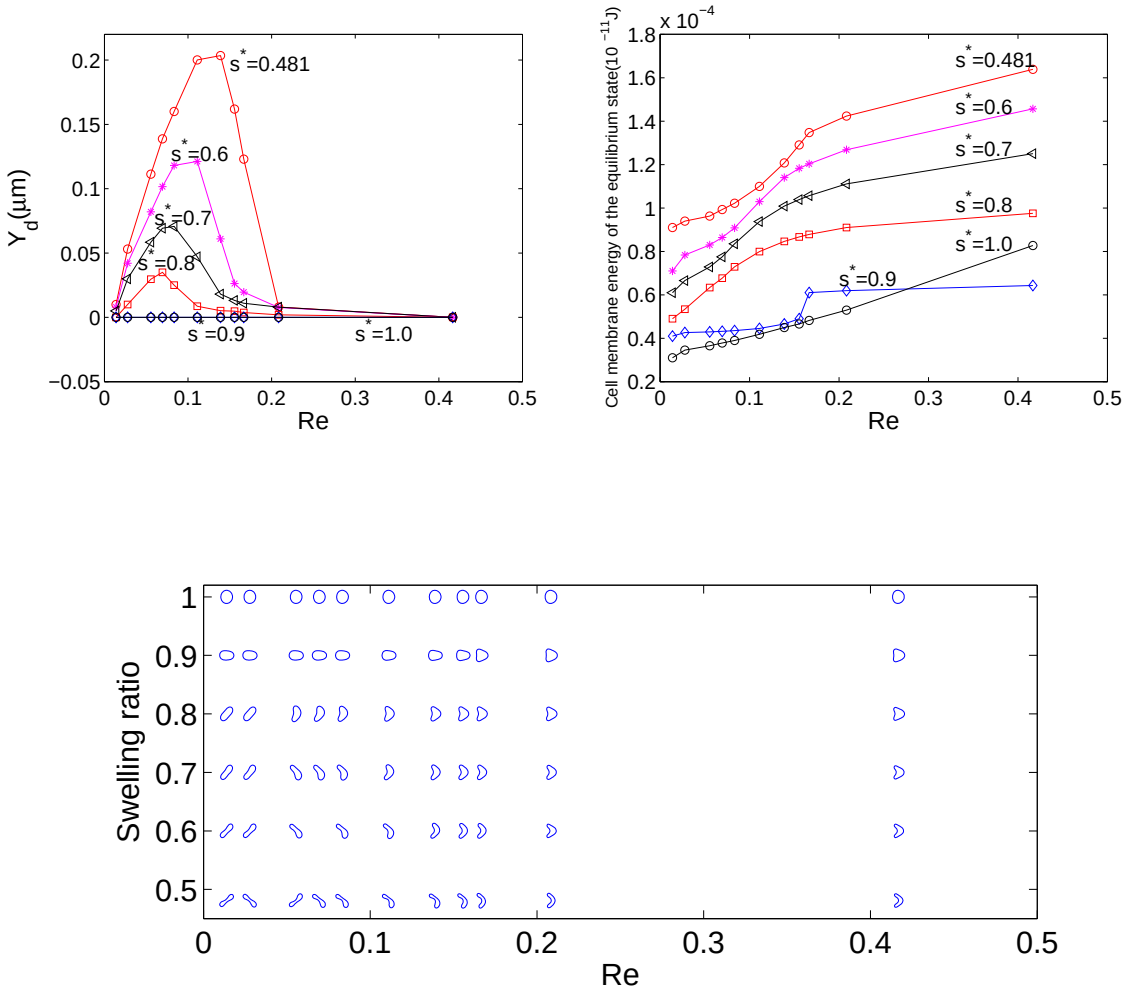

Figure 10: (Color online). The distance Y_d between the cell mass center of the equilibrium position and the centerline of the channel as a function of the Reynolds number Re (top left), the cell membrane energy of the equilibrium position as a function of the Reynolds number Re (top right), and the corresponding equilibrium shapes of the various swelling ratios $s^* = 0.481$, 0.6, 0.7 ,0.8, 0.9, and 1.0 (bottom). $R_0/w = 0.56$.

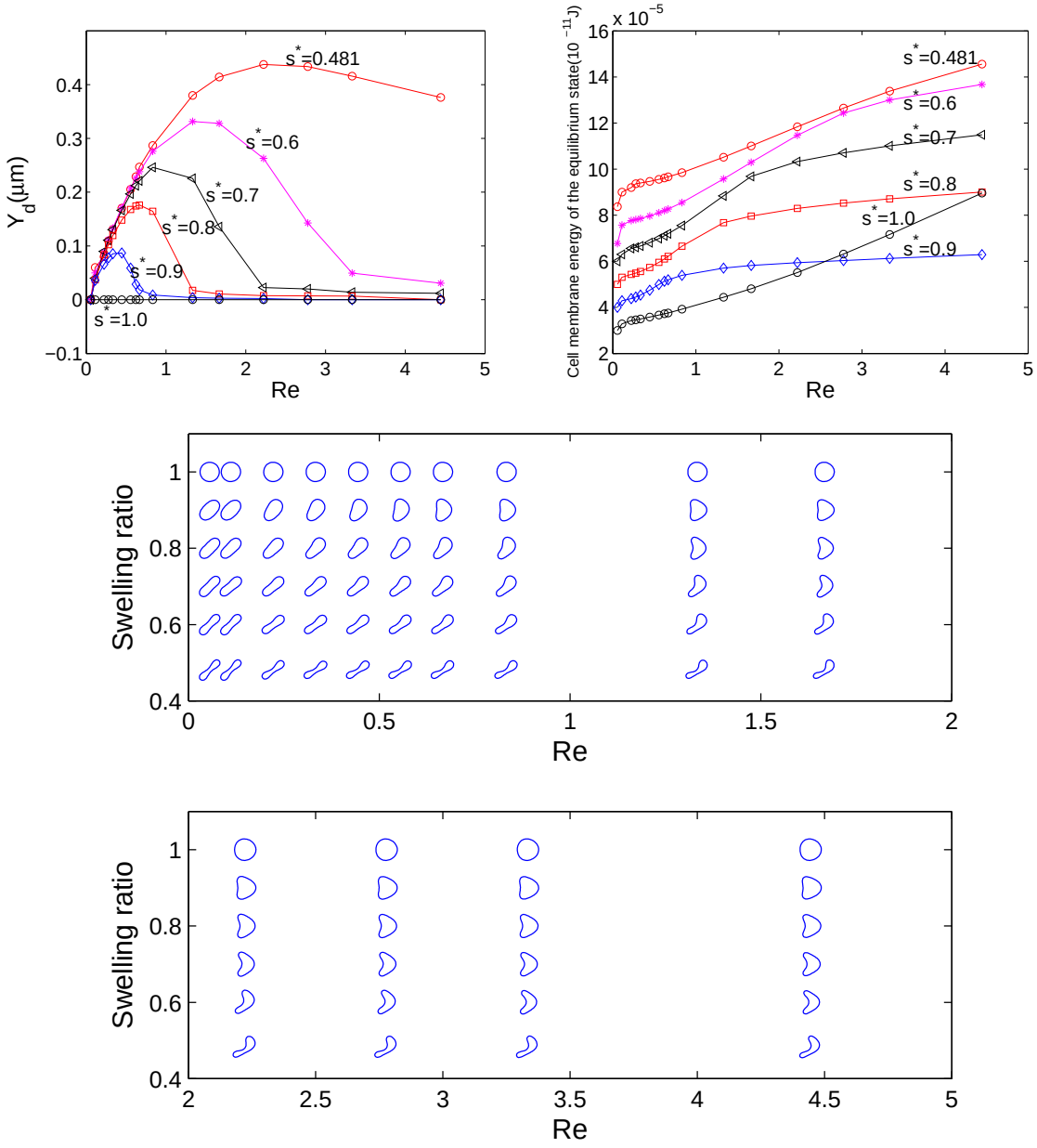

Figure 11: (Color online). The distance Y_d between the cell mass center of the equilibrium position and the centerline of the channel as a function of the Reynolds number Re (top left), the cell membrane energy of the equilibrium position as a function of the Reynolds number Re (top right), and the corresponding equilibrium shapes of the various swelling ratios $s^* = 0.481$, 0.6, 0.7 ,0.8, 0.9, and 1.0 (bottom). $R_0/w = 0.28$.

increasing the Reynolds number Re and reaches a peak, then decreases as increasing Re. The peak of the Reynolds number is a decreasing function of the swelling ratios ($s^* < 1.0$). The distance Y_d is almost zero for s^*=1.0. Given a swelling ratio s^*, the cell membrane energy of the equilibrium position is an increasing function as the Reynolds number Re increases. The slipper shape cell is more stable than the parachute shape one since the energy stored in the former is lower than that in the latter. For a given Re, the bigger the swelling ratio ($s^* < 1.0$), the lower the cell membrane energy. The deformability of cell is harder for the bigger swelling ratio because excess perimeter is less.

Our simulation method has also been applied to the cases of multicells [29, 30]. Studying the migration, deformation and other dynamics of RBCs with the viscosity of the cytoplasm bigger than that of the blood plasma in flow is an interesting and challenging problem and will be done in the near future.

Acknowledgments

This work is supported by an NSF Grant No. DMS-0914788. We acknowledge the helpful comments of James Feng, Ming-Chih Lai and Sheldon X. Wang.

References

[1] T. M. Fischer, *Biophys. J.*, **86**, 3304 (2004).

[2] N. Pamme, *Lab on a chip*, **7**, 1644 (2007).

[3] B. Kaoui, G. Biros, and C. Misbah, *Phys. Rev. Lett.*, **103**, 188101 (2009).

[4] B.P. Ho, and L.G. Leal, *J. Fluid Mech.*, **65**, 365 (1974).

[5] G. Segré, and A. Silberberg, *Nature (London)*, **189**, 209 (1961).

[6] H.L. Goldsmith, *Federation Proc.*, **30**, 1578 (1971).

[7] G. Coupier, B. Kaoui, T. Podgorski, and C. Misbah, *Physics of Fluids*, **20**, 111702 (2008).

[8] G. Segre, and A. Silberberg , *J. Fluid. Mech.*, **14**, 115 (1962).

[9] G. Segre, and A. Silberberg , *J. Fluid. Mech.*, **14**, 136 (1962).

[10] A. Karnis, H.L. Goldsmith, and S.G. Mason, *Nature*, **200**, 159 (1963).

[11] A. Karnis, H.L. Goldsmith, and S.G. Mason, *Can. J. Chem. Engng*, **44**, 181 (1966).

[12] T. Ko, N.A. Patankar, and D.D. Joseph, *Computers and Fluids*, **35**, 121 (2006).

[13] S. Mortazavi, and G. Tryggvason, *J. Fluid Mech.*, **vol. 411**, 325 (2000).

[14] M. Yoshino, and T. Murayama, *Eur. Phys. J.Special. Topics*, **171**, 151 (2009).

[15] C. Pozrikidis, *Ann. Biomed. Eng.*, **33**, 165 (2005)

[16] B. Kaoui, G.H. Ristow, I. Cantat, C. Misbah, and W. Zimmermann, *Phy. Rev. E*, **77**, 021903 (2008).

[17] B. Kaoui, N. Tahiri, T. Biben, H. Ez-Zahraouy, A. Benyoussef, G. Biros, and C. Misbah, *Phy. Rev. E*, **84**, 041906 (2011).

[18] S. J. Shin, and H. J. Sung, *Phys. Rev. E*, **83**, 046321 (2011).

[19] S-D Chen, T-W Pan, and C-C Chang, *Physics of Fluid*, to appear.

[20] L. Shi, T. W. Pan, and R. Glowinski, *Phys. Rev. E*, **85** 016307 (2012).

[21] S. K. Doddi, and P. Bagchi, *Int. J. Mul. Flow*, **34**, 966 (2008).

[22] G. Danker, P. M. Vlahovska, and C. Misbah, *Phys. Rev. Lett.*, **102**, 148102 (2009).

[23] H. B. Li, H. H. Yi, X. M. Shan, and H. P. Fang, *Europhysics Letters*, **81**, 54002 (2008).

[24] K. Tsubota, S. Wada, and T. Yamaguchi, *J. Biomech. Sci. Eng.*, **1**, 159 (2006).

[25] E. J. Dean, and R. Glowinski, *C.R. Acad. Sc. Paris, Série I*, **325**, 783 (1997).

[26] R. Glowinski, *Handbook of Numerical Analysis*, Vol. IX, Ciarlet PG and Lions JL (Eds.), North-Holland: Amsterdam, 7 (2003).

[27] T. W. Pan, and T. Wang, *International Journal of Numerical Analysis and Modeling*, **6**, 455 (2009).

[28] T. W. Pan, and R. Glowinski, *Computational Fluid Dynamics Journal*, **9(2)**, 28 (2000).

[29] T. W. Pan, L. Shi, and R. Glowinski, *Chinese Annals of Mathematics, Series B*, **31**, 975 (2010).

[30] L. Shi, T. W. Pan, and R. Glowinski, *Int. J. Numer. Methods Fluids*, **68**, 1393 (2012).

[31] B. Kaoui, J. Harting, and C. Misbah, *Phys. Rev. E*, **83**, 066319 (2011).

[32] J. Adams, P. Swarztrauber, and R. Sweet, FISHPAK: A package of Fortran subprograms for the solution of separable elliptic partial differential equations, The National Center for Atmospheric Research, Boulder, CO, 1980.

[33] C. S. Peskin, *J. Comput. Phys.*, **25**, 220 (1977).

[34] C. S. Peskin, and D. M. McQueen, *J. Comput. Phys.*, **37**, 11332 (1980).

[35] C. S. Peskin, The immersed boundary method, *Acta Numer.*, **11**, 479 (2002).

[36] C. Pozrikidis *Phys. Fluids*, **17**, 031503 (2005).

[37] T. W. Secomb, and R. Skalak, *Microvasc. Res.*, **24**, 194 (1982).

[38] R. Skalak and P. I. Branemark, *Science*, **164**, 717 (1969).